CivilEng

MDPI

Article

Seismic Response Characteristics of Arch-Type Siphon Bridge Structure Under Pulse-Type Fault-Crossing Ground Motions

Yupeng Ou [1], Pingan Liu [1], Youlin Chen [1], Tiehu Wang [1], Xiang Liu [2] and Xun Zhang [3,*]

[1] Power China Chengdu Engineering Corporation Limited, Chengdu 611130, China; zym2024210087@163.com (Y.O.); sicau12306@163.com (P.L.); cyl2026030266@163.com (Y.C.); 18482066201@163.com (T.W.)
[2] Department of Bridge Engineering, Southwest Jiaotong University, Chengdu 610031, China; xiangliu1997@my.swjtu.edu.cn
[3] State Key Laboratory of Bridge Intelligent and Green Construction, Southwest Jiaotong University, Chengdu 611756, China
* Correspondence: zhxunxun@swjtu.edu.cn

Abstract

Fault-crossing ground motions, characterized by velocity pulses, permanent fault displacement, and non-uniform support excitation associated with fault rupture, may significantly affect the seismic performance of siphon bridges crossing active faults. This study investigates a long-span siphon arch bridge subjected to pulse-type fault-crossing ground motions. A unified stochastic ground motion model is developed by integrating nonstationary high-frequency components based on the evolutionary power spectrum with low-frequency pulse components represented by an improved Gabor wavelet, capturing forward directivity effects, permanent displacement, and differential support input at the two sides of the fault. A three-dimensional nonlinear finite element model is established in OpenSees using fiber-based beam–column elements, with hydrodynamic effects incorporated through the added mass method. Parametric analyses consider pulse phase angle (0–90°), amplitude (Mw 6.0–7.5), and frequency (0–1 Hz). Results indicate that structural responses decrease with increasing phase angle, with 0° being most unfavorable, highlighting the dominant influence of permanent displacement. Resonance amplification occurs when pulse frequencies approach the fundamental modes of the pier (0.345 Hz) and deck (0.51 Hz), while the arch is particularly sensitive near 0.439 Hz. Water added mass reduces natural frequencies by 8–14% and significantly amplifies internal forces. These findings provide guidance for seismic design of fault-crossing siphon bridges.

Keywords: fault-crossing ground motion; siphon arch bridge; seismic response; finite element simulation; sliding effect

Academic Editor: Angelo Luongo

Received: 2 March 2026
Revised: 8 May 2026
Accepted: 15 May 2026
Published: 16 May 2026

1. Introduction

Active fault zones in seismically active regions often intersect rivers, transportation corridors, and urban areas. Lifeline structures such as bridges, siphon systems, and pipelines crossing active faults may experience severe seismic demands because they are simultaneously affected by transient dynamic shaking and quasi-static fault-induced deformation. Previous studies have provided important foundations for understanding such near-fault and fault-crossing motions. Mavroeidis and Papageorgiou [1] proposed a mathematical representation of near-fault velocity pulses, while Mavroeidis et al. [2] further demonstrated that the structural response of elastic and inelastic systems is strongly related to the relationship between the pulse period and the structural period. Bray and Rodriguez-Marek [3] characterized forward-directivity ground motions and emphasized the significance of strong velocity pulses in the near-fault region. In addition to pulse-like dynamic effects, permanent fault displacement is another critical feature of fault-crossing motions. Youngs et al. [4] developed a probabilistic fault displacement hazard analysis framework, and Hisada and Bielak [5] provided a theoretical interpretation of static offset, fling-step effects, and rupture directivity. Beresnev [6] and Rupakhety et al. [7] further contributed to the simulation and quantification of near-fault high-frequency ground-motion characteristics and response spectra. These studies indicate that fault-crossing ground motions should be described by the combined effects of velocity pulses, permanent displacement, and spatially non-uniform support excitation, rather than by conventional far-field seismic input alone. In addition to fault-induced differential support excitation, travelling-wave effects caused by the finite propagation velocity of seismic waves are also an important source of non-uniform seismic input for bridge structures. The wave-passage time delay between different supports may modify the phase relationship of seismic excitation and affect the dynamic response of bridges, especially when spatially varying ground motions and soil–structure interaction are considered [8]. For lifeline systems such as siphon structures, seismic damage may not only interrupt water conveyance but also induce secondary hazards and post-earthquake service disruption [9,10]. Therefore, accurately characterizing fault-crossing ground motions and clarifying the seismic response mechanism of siphon structures are essential for improving the seismic safety and resilience of water-conveyance infrastructure.

Extensive research has been conducted both domestically and internationally on the characterization and modeling of fault-crossing ground motions. Mayssa Dabaghi et al. [11] developed a random model for near-fault ground motion parameters, incorporating two orthogonal horizontal components using the Gabor wavelet model, and investigated the correlation between the two components. Later, Mayssa Dabaghi et al. [12] extended their study to propose a synthesis method for horizontal near-fault components under specific source mechanisms and site conditions, providing a theoretical basis for simulating horizontal near-fault motions. Peng et al. [13] introduced a probabilistic synthesis method based on Copula functions to address the limitations of empirical linear regression methods for random vibration analysis, enabling the simulation of pulse-type random ground motions. To improve the Copula model's accuracy in synthesizing random pulse ground motions, Luo et al. [14] further applied a probability density evolution method. Zhang et al. [15] proposed a near-fault pulse ground motion model based on response spectrum inversion. Jiang et al. [16] presented a three-component synthesis method for pulse ground motions, overcoming the limitation of Mayssa Dabaghi et al.'s method [12], which only synthesized horizontal components, providing a reference for three-component simulation of pulse-type ground motions. Additionally, Luo et al. [17] introduced a fully non-stationary ground motion model, improving the synthesis accuracy of high-frequency components in near-fault pulse motions and enhancing the simulation of permanent displacements in fault-crossing motions. Liu et al. [18] investigated the differences in synthesizing sliding effect and directional effect seismic motions, showing that different types of near-fault motions could be synthesized using a unified formula by altering the pulse period in the mathematical expression, providing a useful reference for simplifying near-fault motion synthesis methods.

Compared with conventional bridges, siphon bridge structures are expected to exhibit different seismic behavior under near-fault and fault-crossing ground motions because the water-conveyance pipeline introduces additional mass and fluid–structure interaction effects. These effects may reduce the structural natural frequencies and modify the distribution of seismic demands, especially when the dominant pulse frequency approaches the vibration modes of the bridge [19]. From the perspective of seismic resilience, the performance of lifeline infrastructure should not be evaluated only by peak structural responses, but also by functionality loss, downtime, recovery process, and restoration capacity. Recent resilience-oriented studies have emphasized that deterioration, damage accumulation, and recovery modeling are key components in evaluating the post-earthquake performance of structures and infrastructure systems [20–22]. For bridge structures, different structural configurations may lead to different seismic fragility and performance levels, which further influence post-event functionality and recovery planning [23]. In this context, siphon bridges are not only structural systems but also water-conveyance lifeline components. Therefore, identifying the critical demand amplification mechanisms under pulse-type fault-crossing ground motions is a necessary step toward resilience-informed seismic design and post-earthquake recovery assessment of siphon bridge systems. Regarding research on siphon arch bridges, Wang et al. [24] conducted shake table tests to investigate the impact of different seismic isolation bearings on the dynamic response of siphon arch bridges under near-fault pulse ground motions. Their results showed that variations in bearing type led to changes in the structural period, resulting in significant differences in internal force responses. Wu et al. [25] also performed shake table tests and analyzed the effects of near-fault pulse parameters on the response of siphon arch bridges, finding that the pulse period predominantly controls the structural response when the low-frequency pulse component dominates. The maximum dynamic strain in the arch typically occurred at one-quarter of the span. Zhou et al. [26] developed a fluid–structure interaction model for siphon bridges using numerical simulations and studied the structural force response under seismic loading. Li et al. [27] compared different siphon pipeline structures crossing active faults, pointing out that siphon engineering structures inevitably cross active faults in practical layouts. Xie et al. [28] demonstrated that water hammer pressure in siphon systems could lead to significant longitudinal deformation of siphon arch bridges. Wang et al. [29] employed finite element methods to analyze the tensile stresses and relative displacements in a shallowly embedded large siphon structure under seismic excitation. Shi et al. [30] established a finite element model for siphon structures, investigating their seismic response and potential dam aging. Jiang et al. [31] studied the seismic response of siphon arch bridges in valley terrains, showing the need for addressing the valley topography effects in the seismic analysis of siphon bridges. In summary, existing studies have made substantial contributions to near-fault ground-motion simulation, pulse-type seismic response analysis, and seismic performance evaluation of siphon arch bridges. However, most available studies on siphon bridges mainly focus on far-field motions, forward-directivity pulse effects, or conventional multi-component seismic input. The combined influence of fault-crossing permanent displacement, velocity-pulse effects, spatially non-uniform support excitation, and water-added mass on siphon arch bridges has not been sufficiently clarified. Moreover, from a resilience-oriented viewpoint, existing studies have rarely linked the demand amplification mechanism of fault-crossing siphon bridges with the service continuity of water-conveyance lifeline systems.

To address these gaps, this paper investigates the seismic response characteristics of an arch-type siphon bridge crossing an active fault. Compared with previous studies, the originality of this work lies in the integration of a fault-crossing stochastic ground-motion model with a three-dimensional nonlinear finite element model of a water-conveyance siphon bridge. The proposed analysis explicitly considers velocity pulses, permanent fault displacement, multi-point support excitation, and water-added mass, and further identifies the most unfavorable pulse phase angle and frequency-sensitive ranges of key structural components. The main contributions are as follows:

(1) A mathematical model for pulse-type fault-crossing ground motions is developed by combining non-stationary high-frequency components with low-frequency pulse components. The model simultaneously accounts for near-fault velocity pulses, permanent fault displacement, and spatially non-uniform support excitation, providing a unified seismic input framework for fault-crossing lifeline structures.
(2) A three-dimensional nonlinear finite element model of a typical siphon arch bridge is established with consideration of the water-added mass effect. Based on this model, the effects of pulse phase angle, pulse amplitude, pulse frequency, and water mass on displacement demands and internal force redistribution are systematically investigated, providing a technical basis for seismic design and future resilience-oriented assessment of fault-crossing siphon bridge systems.

2. Project Overview and Finite Element Modeling

The region exhibits significant tectonic activity, with relatively poor structural stability. Given the project's unique geographic location, the likelihood of seismic influence during its operation is high. Geological investigations indicate that the project site is located along an active fault zone, and the siphon bridge structure directly crosses the fault. To mitigate the potential adverse effects of near-fault sliding and other seismic hazards on the bridge structure, it is essential to conduct seismic analysis for fault-crossing scenarios.

A three-dimensional nonlinear finite element model of the bridge was established in OpenSees [32]. The main beam was modeled using elastic beam–column elements, while the arch rib and the vertical supports were modeled using force-based beam–column elements with fiber sections, so that the sectional nonlinear behavior of the main load-carrying members could be represented. The concrete constitutive behavior was simulated using the Concrete02 material based on the modified Kent–Park model [33]. The mass of the bridge deck and siphon pipeline was assigned to the corresponding deck nodes. The hydrodynamic effect of the water inside the pipeline was simplified by the added-mass method and applied to the same nodes. To represent the simply supported connection between the bridge deck and the vertical supports, ZeroLength elements were introduced at the pier–beam connection locations [34]. The general layout, coordinate system, fault location, and key structural sections of the siphon arch bridge are shown in Figure 1.

The mass of the bridge deck and siphon pipeline was assigned to the corresponding deck nodes. The hydrodynamic effect of the water inside the pipeline was simplified by the added-mass method and applied to the same nodes. The added mass of water was calculated as follows:

$$m_w = \rho \pi R^2 L \tag{1}$$

where m_w is the added mass of water in the pipeline, ρ is the density of water, R is the radius of the pipeline, and L is the element length. In the present preliminary study, the bridge foundation was assumed to be rigid, and soil–structure interaction (SSI) was neglected in order to focus on the global response characteristics of the siphon arch bridge under fault-crossing pulse-type ground motions. However, this simplification does not account for the possible influence of foundation flexibility, soil-induced modification of seismic input, or local redistribution of deformation and internal forces near the supports. Therefore, the present results should be interpreted as those obtained under the rigid-foundation assumption, and a more refined model including SSI will be considered in future work. The above modeling strategy, material model, boundary treatment, and mass assignment procedure were consistently used in all subsequent analyses.

https://doi.org/10.3390/civileng7020032

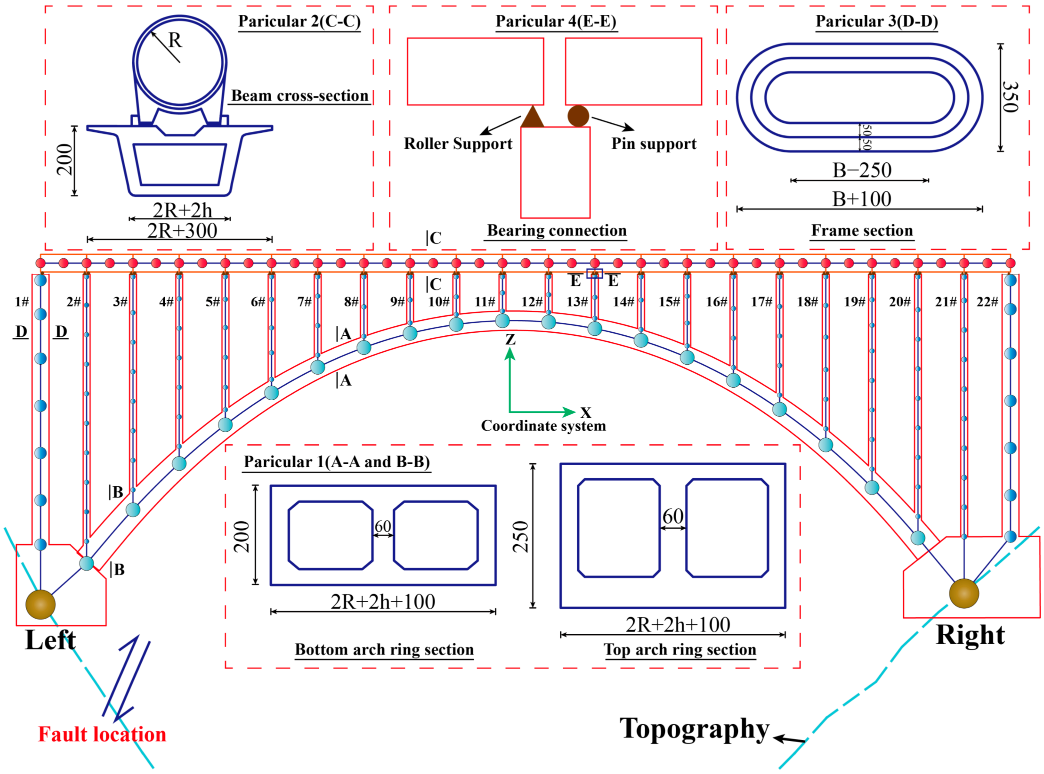

Figure 1. General Layout (Unit: mm).

Through eigenvalue analysis in OpenSees, version 3.8.0. The natural frequencies and vibration modes of the siphon arch bridge were obtained and cross-checked using Midas Civil, version 2026. In order to verify the reasonableness of the numerical model before conducting the parametric seismic-response analysis. The results, shown in Figure 2, indicate that for the bridge with no water, the first five natural frequencies are 0.369 Hz, 0.369 Hz, 0.487 Hz, 0.542 Hz, and 0.552 Hz, respectively. When the pipeline is full of water, the first five natural frequencies are 0.326 Hz, 0.326 Hz, 0.445 Hz, 0.475 Hz, and 0.484 Hz. The coincidence of the first two frequencies is mainly attributed to the high geometric and stiffness symmetry of the bridge system, which leads to a pair of nearly degenerate modes with very similar generalized stiffness and mass characteristics. The added mass of the water causes a reduction of about 8–14% in the structure's natural frequency. The first and second modes correspond to longitudinal bending vibration of the vertical arch supports, the third mode corresponds to lateral vibration of the arch ring, and the fourth and fifth modes correspond to longitudinal bending vibrations of the vertical arch supports. From the eigenfrequency analysis, it is observed that pulse-type earthquakes typically have low frequencies and long periods, with frequencies close to the natural frequencies of the siphon arch bridge. This can lead to resonance phenomena in the bridge [24]. Therefore, the modal analysis not only serves as a basic validation of the numerical model, but also provides the dynamic basis for the subsequent investigation of the adverse effects of pulse-type earthquake parameters on the structural performance of the bridge.

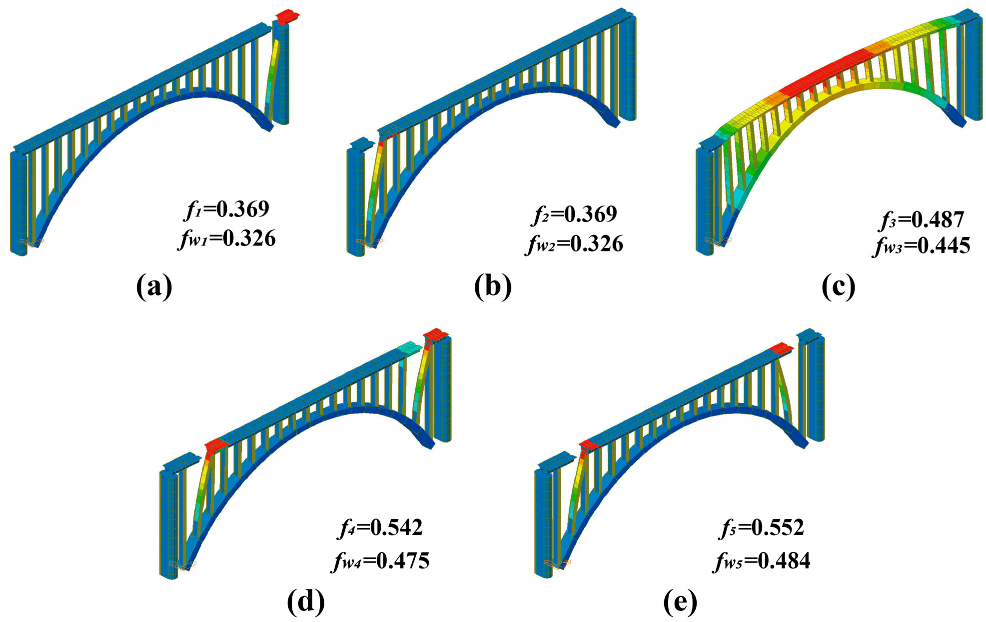

Figure 2. First Five Vibration Modes: (**a**) First Mode; (**b**) Second Mode; (**c**) Third Mode; (**d**) Fourth Mode; (**e**) Fifth Mode.

3. Fault-Crossing Ground Motion Mathematical Model

The sliding effect primarily occurs in the direction of fault movement along strike-slip or thrust-slip faults. In the case of thrust-slip fault earthquakes, both the directional effect and the sliding effect act on the fault. When permanent displacement coincides with the maximum ground displacement during the seismic vibrations, the level of seismic damage is significantly increased [35].

3.1. Fault-Crossing Ground Motion Model

Simulation of fault-crossing seismic motions can be divided into high-frequency and low-frequency components. The high-frequency component is synthesized using power spectral functions, while the low-frequency component is modeled using Gabor functions to simulate pulses. These high-frequency and low-frequency time histories are then combined over the entire time domain to generate the fault-crossing ground motion. Specifically, this study adopts the non-stationary ground motion reduction model proposed by Liu et al. [36] for analysis, with the model's detailed expression given as follows:

$$f(t) = \sum_{n=1}^{N} \sqrt{2S_{f_a}(t,\omega_n)\Delta\omega}[\cos(\omega_n t)X_n + \sin(\omega_n t)Y_n] \tag{2}$$

$$S_{f_0}(t,\omega) = A(t)^2 S(\omega) \tag{3}$$

In the equation, $f(t)$ represents a non-stationary process, X_n and Y_n are orthogonal random variables, S_{f_0} is the evolution power spectrum, and $A(t)$ is the time modulation function, where N denotes the truncation term.

The time modulation function is used to modulate the duration of the earthquake and can be expressed as:

$$A(t) = \left[\frac{t}{c}\exp\left(1-\frac{t}{c}\right)\right]^d \tag{4}$$

In the equation, c represents the average time at which the peak acceleration of the ground motion occurs, and d is the exponent controlling the shape.

The Kanai–Tajimi spectrum is used to simulate $S(\omega)$ which can be expressed as [37]:

$$S(\omega) = \frac{\omega^4{}_g + 4\zeta_g^2\omega_g^2\omega^2}{\left(\omega^2 - \omega_g^2\right)^2 + 4\zeta_g^2\omega_g^2\omega^2} \cdot S_0 \tag{5}$$

In the equation, ω_g and ζ_g represent the angular frequency and damping ratio of the site soil, respectively. S_0 is the spectral intensity factor of the stationary ground motion, which can be expressed as:

$$S_0 = 2 \cdot \frac{A^2{}_{\max}}{\gamma^2\pi\omega_g\left(2\zeta_g + \frac{1}{2\zeta_g}\right)} \tag{6}$$

In the equation, $A_{\max}$ represents the average value of the peak ground acceleration, and γ denotes the peak factor of the stationary ground motion.

For the low-frequency pulse model, the modified Gabor wavelet function proposed by Liu et al. [18] is used for simulation, and the expression is given as:

$$a(t) = \begin{cases} -\frac{\pi \cdot PGV}{\gamma_v T_p}\left[\begin{array}{l} \sin\left(\frac{2\pi}{\gamma_v T_p}(t-t_0)\right)\cos\left[\frac{2\pi}{T_p}(t-t_0)+\varphi\right] \\ +\gamma_v \sin\left[\frac{2\pi}{T_p}(t-t_0)+\varphi\right]\left[1+\cos\left(\frac{2\pi}{\gamma_v T_p}(t-t_0)\right)\right] \end{array}\right], & t_0 - \frac{\gamma T_p}{2} \le t \le t_0 + \frac{\gamma T_p}{2} \\ & with\ \gamma_v > 1 \\ 0, \quad otherwise & \end{cases} \tag{7}$$

In the equation, $a(t)$ represents the artificially synthesized acceleration pulse time history, PGV is the pulse peak, T_p is the pulse period, φ is the pulse phase angle, γ_v is the number of pulse periods, and t_0 is the moment at which the peak of the low-frequency velocity pulse occurs.

The relationship between pulse period and magnitude [18] can be expressed as:

$$\ln T_p = -5.45 + 0.97\ Mw \tag{8}$$

The relationship between pulse peak, magnitude, and fault distance [18] can be expressed as:

$$\ln PGV = 2.56 + 0.23\ Mw - 0.19 \ln R_{rup} \tag{9}$$

In the equation, Mw represents the magnitude, and R_{rup} represents the fault distance.

Liu et al. [18] calculated that the range of pulse periods for fault-crossing seismic motions is [1, 2), and they clarified the effect of changes in the pulse phase angle on the permanent displacement caused by near-fault sliding effects. Additionally, Tang et al. [38] noted that the arrival time of the pulse should correspond to the peak of the high-frequency acceleration time history, i.e., the pulse arrival time should fall within the flat section of the modulation function. Shahi and Baker [39,40] also emphasized in their studies that if the pulse arrives too early, it may cause the entire seismic motion to lose its pulse characteristics. The parameter values for the high-frequency acceleration expression can be referred to in [41].

In this study, a full-time-domain high–low frequency superposition method is adopted to synthesize the fault-crossing ground motion. The high-frequency component is generated from the evolutionary power spectrum and is used to represent the nonstationary random fluctuation of the ground motion. The low-frequency component is generated using the improved Gabor wavelet method and is used to represent the long-period pulse and permanent-displacement-related characteristics of fault-crossing seismic motions. The two components are then superimposed over the entire time domain to obtain the synthesized fault-crossing acceleration time history. In this way, the final input motion can simultaneously reflect the random high-frequency content and the low-frequency pulse characteristics of fault-crossing ground motions. The specific expression for the high-low frequency superposition is given as [42]:

$$a(t) = a_h(t) + a_p(t) \tag{10}$$

In the equation, $a_h(t)$ represents the high-frequency component of the acceleration time history, $a_p(t)$ represents the low-frequency component, and $a(t)$ denotes the artificially synthesized fault-crossing seismic acceleration time history obtained from the superposition of the high and low-frequency components.

3.2. Fault-Crossing Ground Motion Synthesis

This study investigates the differences in seismic input for fault-crossing ground motions. For clarity, the original fault-based horizontal components can be interpreted in terms of fault-parallel and fault-normal directions, while the structural response is evaluated in the bridge-fixed coordinate system. In the present case, because the rupture propagation direction is assumed to be orthogonal to the bridge axis, the fault-displacement-dominated component is projected mainly onto the bridge transverse direction, whereas the pulse-type directional component is projected mainly onto the bridge longitudinal direction. Specifically, when a fault undergoes rupture, if the fault's interior side is defined as the rupture propagation direction, the soil on one side of the fault will move along the rupture direction, while the soil on the opposite side will move in the opposite direction [34]. Therefore, for the case outlined in this study, as shown in Figure 1, when the rupture direction is orthogonal to the bridge axis, the left abutment will experience a lateral displacement curve due to sliding effects, as shown in Figure 3a, while the right abutment will experience a lateral displacement curve as shown in Figure 3b. Figure 3 also illustrates the impact of phase angle variations on the sliding effect displacement time history. As the phase angle changes, the lateral displacement varies with the angle between the phase angle and the bridge axis [35]. When the phase angle is 0°, the permanent displacement reaches its maximum, while at 90°, the lateral permanent displacement is nearly zero.

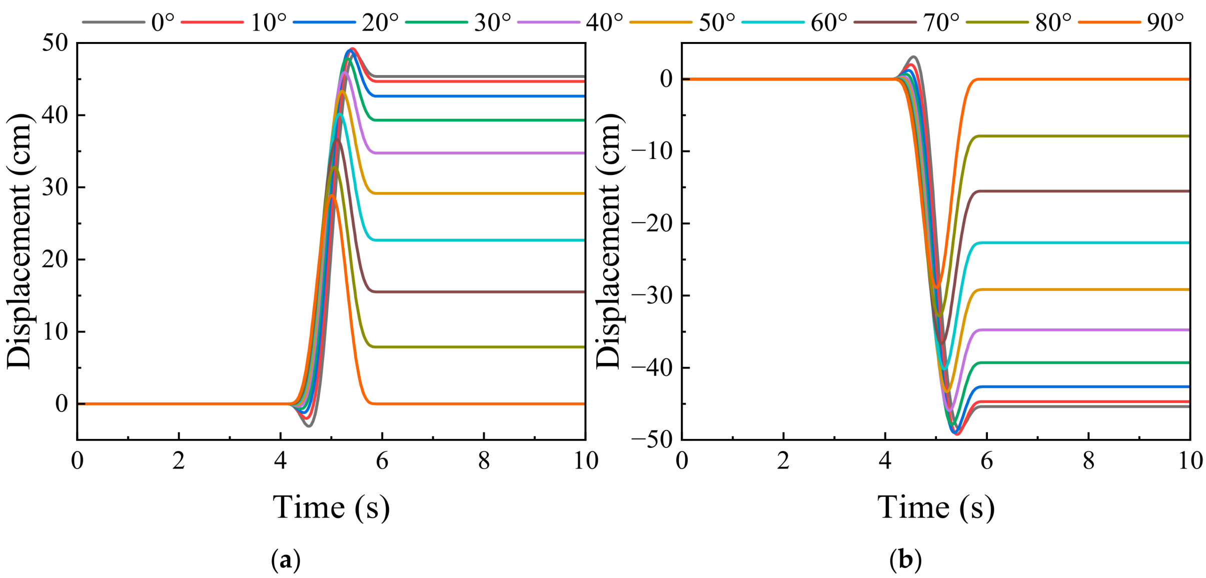

Figure 3. Lateral Seismic Time History Displacement Curve: (**a**) Left; (**b**) Right.

For longitudinal seismic displacement, fault rupture generates significant directional pulse effects. Although no permanent displacement is formed in the longitudinal direction, prominent velocity pulses are induced [35]. Therefore, the longitudinal ground motion can be treated as a pulse time history with directional effects. In this case, the number of pulse periods in Equation (8) is set to a value greater than 2 to simulate the directional pulse seismic motion time history, as shown in Figure 4. For vertical ground motion input, it is treated as a seismic motion time history without pulse components, and the high-frequency component is directly used for calculations.

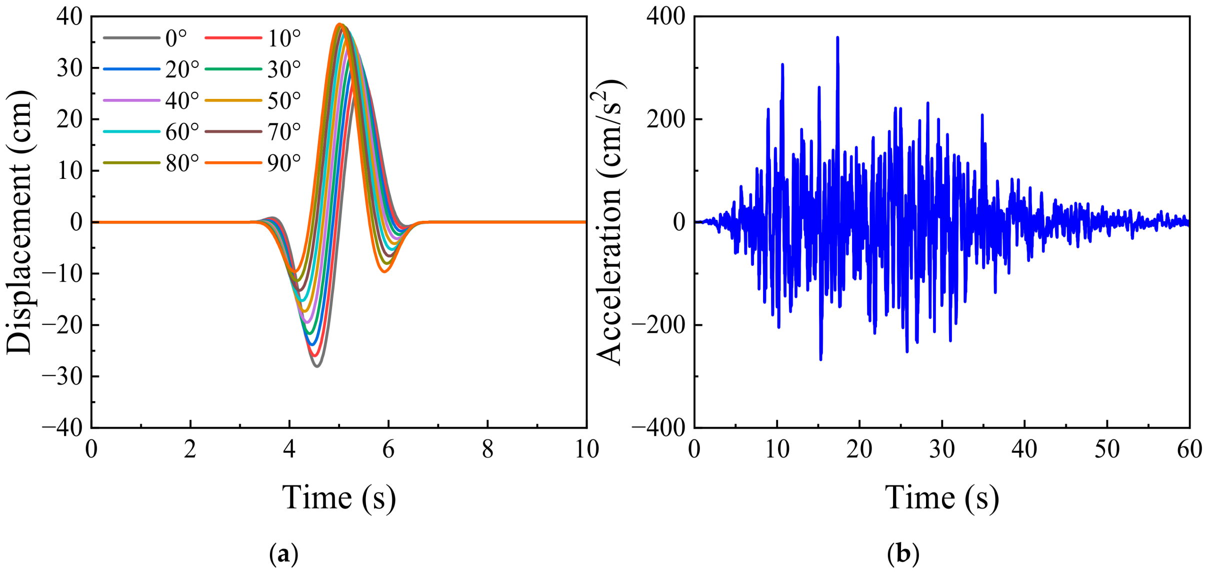

Figure 4. Seismic Time History Curves: (**a**) Longitudinal; (**b**) Vertical.

According to the geological survey report, the site is classified as Category II, so the calculation of the high-frequency component uses the first set of design earthquake parameters. The basic seismic intensity in the engineering area is VIII, and the peak ground acceleration for the design earthquake is taken as 0.20 g. Based on these conditions and the relevant provisions of the "Seismic Design Code for Hydraulic Structures" (GB 51247-2018) [43] the high-frequency seismic target response spectrum for this case study is determined, as shown in Figure 5. Figure 5a compares the target response spectrum with the results of the high-frequency seismic motion synthesis method described in Section 3.1. By adjusting the synthetic seismic acceleration through response spectrum matching, the high-frequency component is made to comply with the seismic motion characteristics specified by the code. Figure 5b presents a comparison of the high-frequency acceleration time histories before and after optimization. The optimized high-frequency component is then combined with the low-frequency component in the full-time domain using Equation (10), resulting in the corresponding fault-crossing ground motion model.

It should be noted that Figure 5 is used only to demonstrate the response-spectrum matching of the high-frequency component before the high–low frequency superposition. Therefore, the velocity-pulse feature is not expected to be clearly observed in Figure 5b. The pulse characteristics are introduced by the low-frequency Gabor wavelet component and become evident only after the full-time-domain superposition of the high- and low-frequency components. Accordingly, the pulse-containing motion should be interpreted together with the longitudinal pulse time history shown in Figure 4 and the superposition procedure expressed in Equation (10).

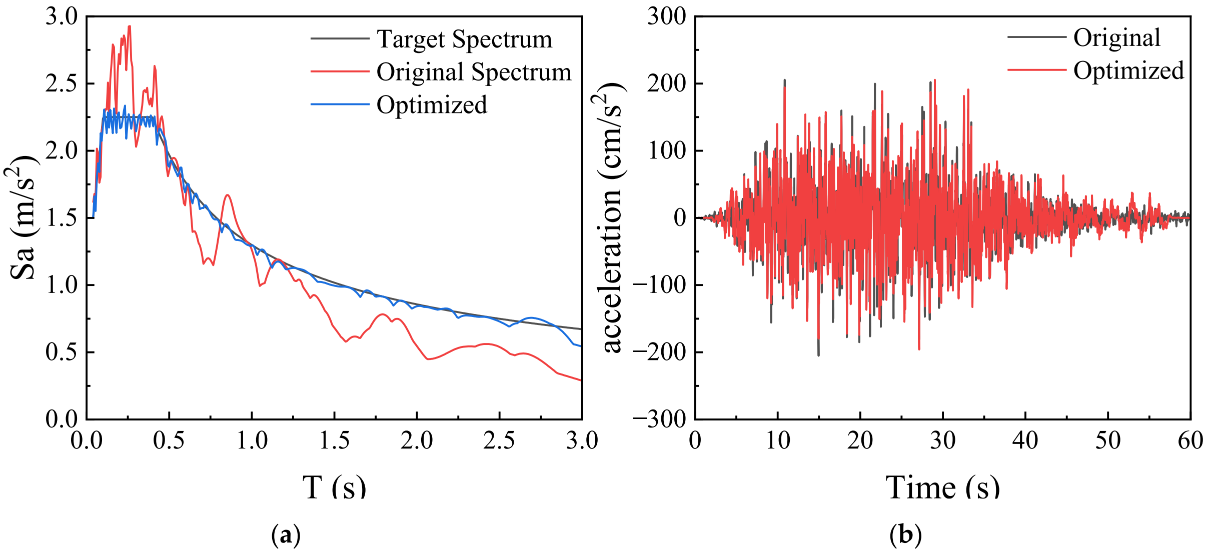

Figure 5. Response-spectrum matching of the optimized high-frequency ground-motion component before high–low frequency superposition: (**a**) comparison of target and synthesized response spectra; (**b**) acceleration time histories before and after optimization.

4. Impact of Pulse Parameters on the Response of Siphon Arch Bridge Structures

4.1. Definition of Pulse Parameters

This section systematically analyzes the impact of pulse parameters on the seismic performance of siphon arch bridge structures, focusing on key parameters such as pulse phase angle, pulse peak, and pulse period, and their mechanisms influencing the seismic response characteristics of the bridge.

First, regarding the effect of pulse phase angle, the internal force response and overall deformation patterns of the bridge under different permanent displacement conditions are analyzed to identify the most adverse pulse phase angle scenario for the structure. The phase angle varies from 0° to 90°, with intervals of 10°, resulting in 10 calculation scenarios. Next, the effect of pulse peak is examined, focusing on the nonlinear characteristics of the seismic response caused by variations in the pulse peak. The sensitivity of the bridge response to increasing seismic magnitude is analyzed, revealing the impact mechanisms of magnitude and fault distance on the bridge's seismic performance. In the relevant scenarios, the magnitude ranges from 6.0 to 7.5, with increments of 0.5, resulting in 4 calculation scenarios. Finally, for the effect of pulse frequency, the study examines both the resonance-sensitive range near the dominant structural frequencies and a broader non-resonant range, in order to explore the response sensitivity of the bridge to pulse-like low-frequency input. By comparing the structural response in different periods, the study further reveals the sensitivity of the siphon arch bridge to low-frequency pulse ground motions. The pulse frequency is varied from 0 to 1 Hz with an increment of 0.05 Hz for the purpose of parametric sensitivity analysis.

4.2. Effect of Pulse Phase Angle

Figures 6 and 7 show the internal force and displacement responses of the siphon arch bridge under different phase angle conditions. Here, the reported "lateral" response components refer to the out-of-plane direction of the arch ring, whereas the "vertical" response components refer to the in-plane vertical direction, with reference to the global coordinate system shown in Figure 1. Under three-directional seismic loading, the axial force and vertical shear force responses are primarily concentrated on the left side of the structure. The maximum internal force occurs at the left arch bottom, with the minimum axial force at 4/9l on the right side, and the minimum vertical shear force at 2/3l on the right side. Lateral shear force varies significantly with phase angle, and as the phase angle increases, the lateral internal force decreases overall, with the maximum lateral response occurring at the arch top and the minimum at 1/3l. Torsional response is lowest at 5/9l and 4/9l, with the maximum torsional response occurring at the arch bottom. Overall, the torsional response decreases gradually as the phase angle increases. This trend can be attributed to the reduction in the transverse permanent-displacement component associated with the sliding effect as the phase angle increases. When the phase angle is close to 0°, the transverse permanent displacement is larger, which induces stronger asymmetric deformation and torsional demand in the arch ring. As the phase angle approaches 90°, the transverse permanent-displacement component becomes much smaller, and the torsional response is correspondingly reduced. This interpretation is consistent with previous studies showing that permanent fault displacement and near-fault sliding effects may govern the displacement demand and local force concentration of structures crossing active faults [17,34]. The maximum lateral bending moment occurs at the arch bottom, while the bending moments at 2/9l, 1/3l, and the arch top are smaller. The bending moment at 5/9l is most sensitive to lateral shear force variation. Vertical bending moment decreases from the arch bottom to the arch top, with its magnitude decreasing as the phase angle increases.

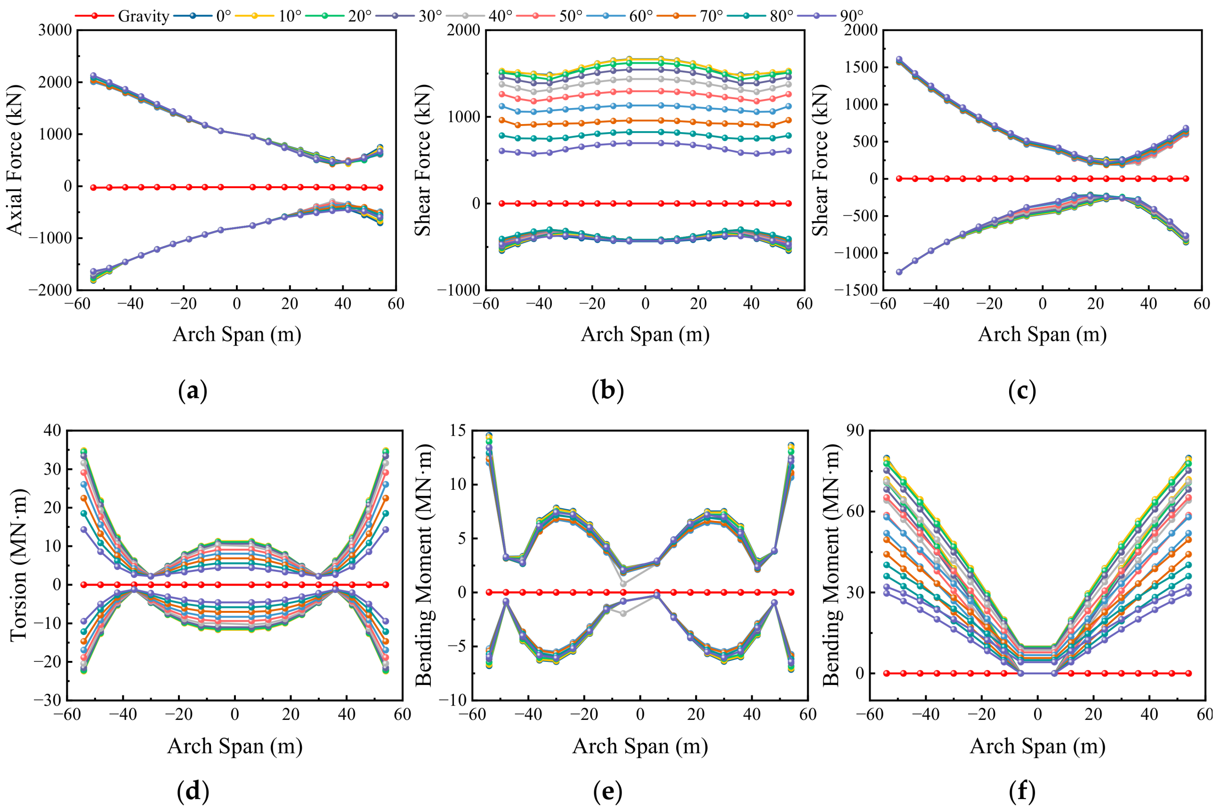

Figure 6. Arch Ring Internal Force Response at Different Phase Angles: (**a**) Axial Force; (**b**) Lateral Shear Force; (**c**) Vertical Shear Force; (**d**) Torsion; (**e**) Lateral Bending Moment; (**f**) Vertical Bending Moment.

The displacement response of the arch ring is shown in Figure 7. Longitudinal displacement is greatest at 1/2l, and lateral displacement decreases from the arch bottom to the arch top, with the displacement at the arch top being near zero. Vertical displacement is greatest at 1/2l, with displacement at the arch bottom and arch top close to zero. Both longitudinal and lateral displacement peak values decrease as the phase angle increases.

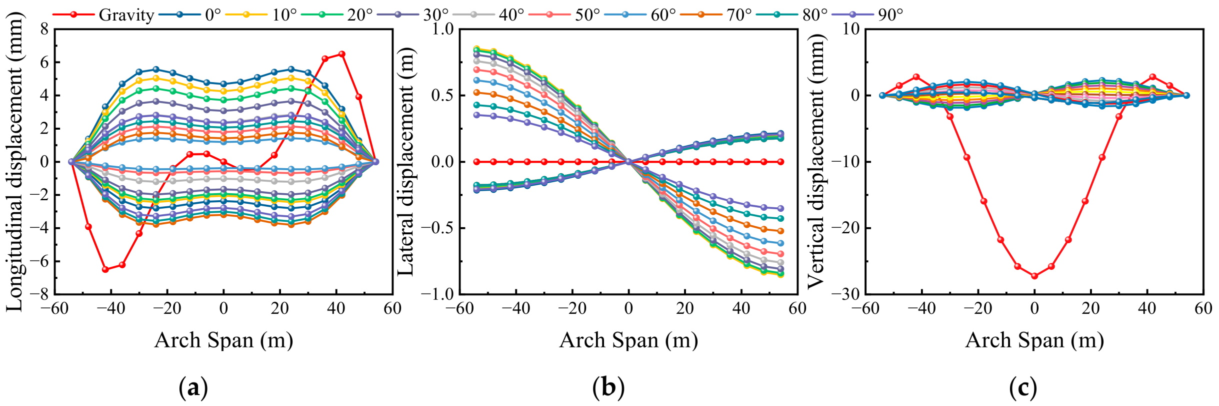

Figure 7. Arch Ring Displacement at Different Phase Angles: (**a**) Longitudinal Displacement; (**b**) Lateral Displacement; (**c**) Vertical Displacement.

Because the first few vibration modes of the siphon arch bridge primarily correspond to the 2# and 3# pier modes, as shown in Figure 8, the longitudinal and lateral displacement responses of the arch supports are largest at 2# pier, gradually decreasing as the phase angle increases. The vertical deformation of the arch supports coincides with the vertical deformation of the arch ring.

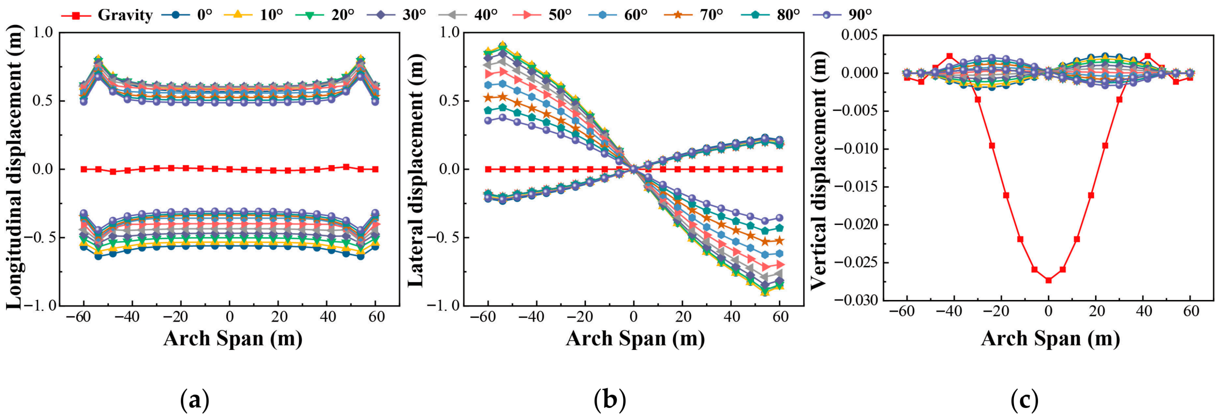

Figure 8. Vertical Support Displacement at Different Phase Angles: (**a**) Longitudinal Displacement; (**b**) Lateral Displacement; (**c**) Vertical Displacement.

As shown in Figure 9, the longitudinal displacement of the main beam is greatest at the second span on the left side and the first span on the right side. Lateral and vertical displacements correspond with the vertical deformation of the piers, and the main beam displacement decreases as the phase angle increases. Overall, as the pulse phase angle increases, the internal force and displacement responses of the siphon arch bridge decrease, with the maximum response occurring at a phase angle of 0° and the minimum at 90°. This indicates that under fault-crossing seismic action, the permanent displacement magnitude of the fault plays a dominant role in the structural response. Based on the distribution characteristics of internal forces and displacements, the key control sections for the seismic analysis of the siphon arch bridge are identified in this study.

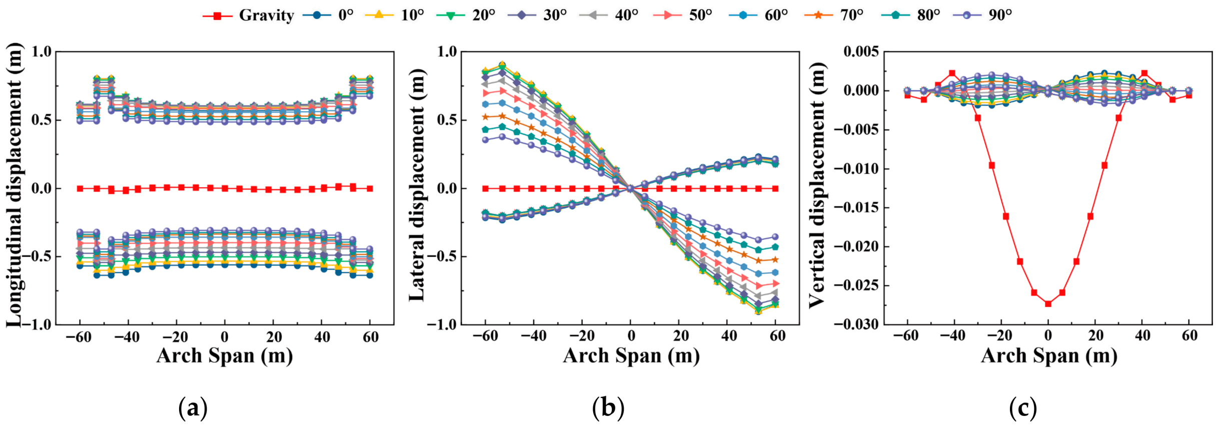

Figure 9. Main Beam Deformation at Different Phase Angles: (**a**) Longitudinal Displacement; (**b**) Lateral Displacement; (**c**) Vertical Displacement.

4.3. Impact of Pulse Peak and Pulse Period

This section further compares the frequency-sensitive ranges of the siphon arch bridge structure under pulse-type seismic motions and examines the influence of seismic magnitude on the structural response. In the calculations, only the effect of magnitude on the pulse peak is considered, while its impact on the pulse period is not included.

It should be noted that the ratio between the bridge fundamental period and the pulse period is an important indicator for pulse–structure resonance, but it is not the only governing parameter for fault-crossing pulse-type ground motions. For a given bridge model, the structural periods remain fixed, and varying the pulse frequency is equivalent to varying the pulse period and hence the corresponding period ratio. Therefore, the pulse-frequency analysis in this section can also be interpreted from the viewpoint of the bridge-period-to-pulse-period relationship. However, for fault-crossing ground motions, the pulse phase angle and pulse peak are also important parameters: the former affects the magnitude of permanent fault displacement and differential support excitation, while the latter controls the intensity level of the pulse component. Therefore, this study retains pulse phase angle, pulse peak, and pulse frequency as independent parameters in the parametric analysis.

Figure 10 shows the effect of pulse frequency variations on the longitudinal and lateral displacement responses of the structure. Figure 10a indicates that, under longitudinal forward directional pulse seismic loading, when the pulse frequency is 0.04 Hz, the displacement at the arch top is significantly amplified. However, no significant amplification is observed at the frequencies of the first ten modes. Figure 10b shows that, under lateral sliding pulse seismic loading, when the pulse frequency is 0.02 Hz, the displacement at the arch top reaches its peak and gradually decreases as the frequency increases. When the pulse frequency approaches the third mode frequency of 0.439 Hz, the response increases again, continuing until it stabilizes near the ninth mode frequency of 0.829 Hz. Combining the participation mass and mode direction factor reveals that the third and ninth modes represent lateral symmetric modes. In conclusion, the pulse frequency-sensitive range of the main arch is primarily near the lateral dominant mode frequency.

Figure 11 shows the resonance frequency range for the vertical supports of the arch. The vertical supports primarily experience longitudinal resonance, with no lateral resonance. The resonance frequencies mainly occur at the first and fourth mode frequencies, consistent with the corresponding mode deformations. Specifically, when the pulse frequency is 0.345 Hz, the 2# support resonates, and when the frequency is 0.51 Hz, the 3# support resonates. Therefore, the pulse frequency-sensitive range for the vertical supports is primarily near the longitudinal dominant mode frequency.

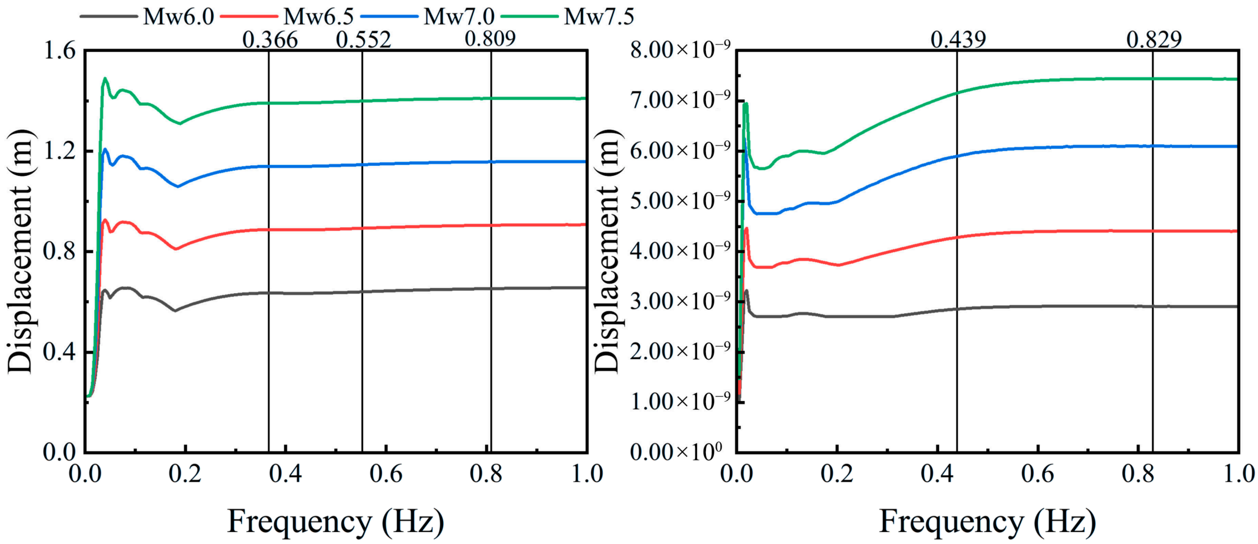

(**a**) (**b**)

Figure 10. Effect of Pulse Frequency and Pulse Peak on Arch Top Displacement: (**a**) Longitudinal Displacement at Arch Top; (**b**) Lateral Displacement at Arch Top.

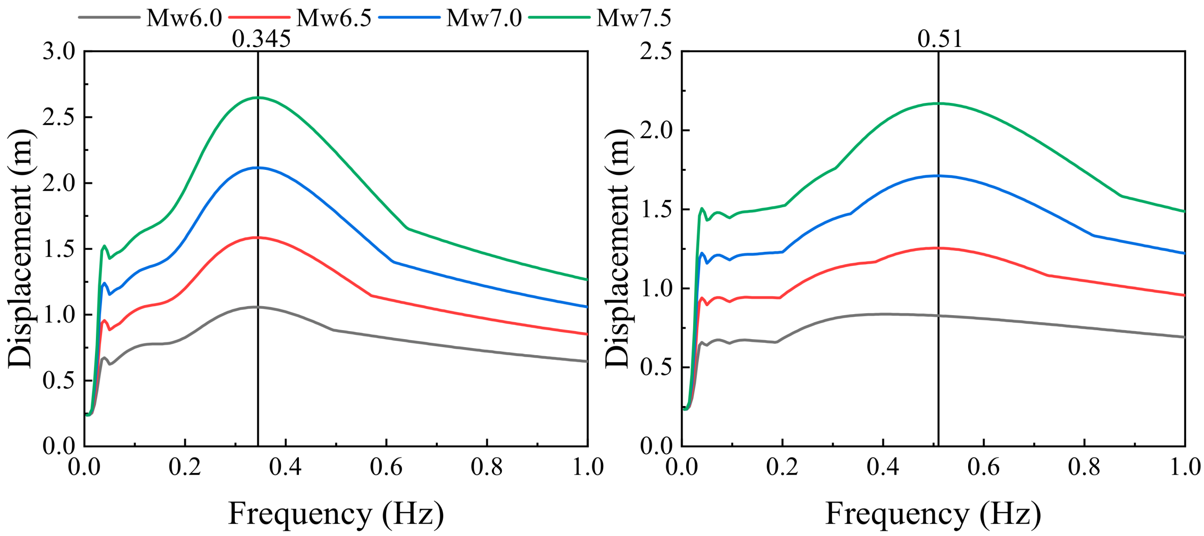

(**a**) (**b**)

Figure 11. Effect of Pulse Frequency and Pulse Peak on Vertical Support Displacement: (**a**) Longitudinal Displacement of 2# Frame; (**b**) Longitudinal Displacement of 3# Frame.

Figure 12 illustrates the resonance frequency range for the main beam. The main beam primarily experiences longitudinal resonance, with no lateral resonance. Resonance frequencies also appear in the first and fourth modes, consistent with the corresponding mode deformations. Specifically, when the pulse frequency is 0.345 Hz, the main beam at the second span resonates, and when the frequency is 0.51 Hz, the main beam at the third span resonates. Therefore, the pulse frequency-sensitive range for the main beam is primarily near the longitudinal dominant mode frequency.

In conclusion, the components of the siphon arch bridge that are sensitive to pulse frequency under fault-crossing seismic motions are primarily the vertical supports and the main beam, which is closely related to the configuration of the siphon structure. The first five modes predominantly exhibit longitudinal deformation, with only the third mode showing lateral symmetric deformation. The main beam and vertical supports primarily resonate through longitudinal mode deformations, indicating that the resonance characteristics of the siphon bridge are influenced by the structural configuration. Based on the analysis, the most unfavorable condition for the fault-crossing seismic action on the siphon structure occurs when the phase angle is 0°. As the magnitude increases, the pulse peak becomes larger, and the structural response strengthens. The resonance range of the siphon bridge is related to the bridge's resonance frequencies, with the main arch primarily experiencing lateral resonance, and the vertical supports and main beam primarily experiencing longitudinal resonance. The resonance ranges are associated with the first ten natural frequencies of the bridge.

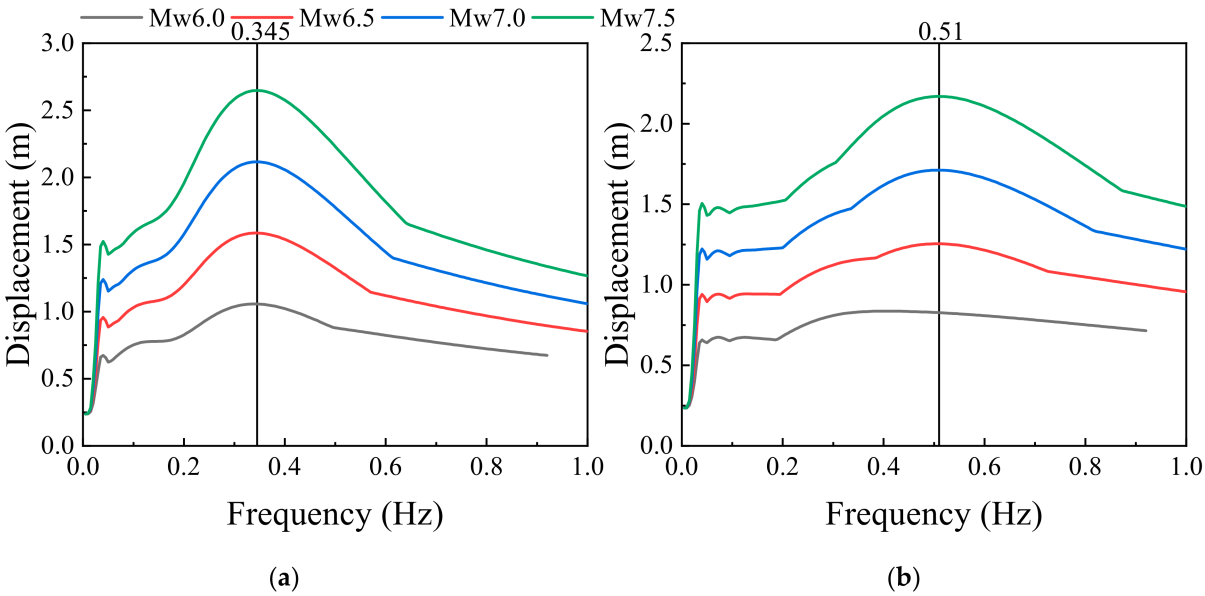

Figure 12. Effect of Pulse Frequency and Pulse Peak on Main Beam Displacement: (**a**) Longitudinal Displacement of the Main Beam at the 2nd Span; (**b**) Longitudinal Displacement of the Main Beam at the 3rd Span.

5. Impact of Water Mass in the Pipeline and Seismic Pulse Effects

Through the analysis in Section 4, this study identifies the most unfavorable condition for the siphon bridge structure under fault-crossing seismic action and performs a comparative analysis based on this condition. The three considered scenarios are: a full water condition in the siphon pipeline, no water in the pipeline, and a full water condition under non-pulse seismic excitation. Figure 13 presents the internal force analysis results for the arch ring under these three scenarios. The results show that the added mass of water in the pipeline significantly increases the internal forces in the arch ring. In the full water condition, compared to the no water condition, the maximum forces in the three translational directions (axial force, lateral shear, and vertical shear) increased by factors of 0.292, 0.066, and 2.38, respectively. The maximum forces in the three rotational directions (torsion, lateral bending moment, and vertical bending moment) increased by factors of 0.218, 0.559, and 0.309, respectively. The internal force variation in the siphon arch structure under the two water conditions shows a consistent trend, with amplification effects observed at key sections. Specifically, the axial force and vertical shear force increase across the entire section, while lateral shear is concentrated at the arch top and arch bottom sections. Torsion and vertical bending moments are slightly amplified by the presence of water, while lateral bending moments increase across the full section. In conclusion, the added water in the pipeline significantly alters the force distribution in the arch ring.

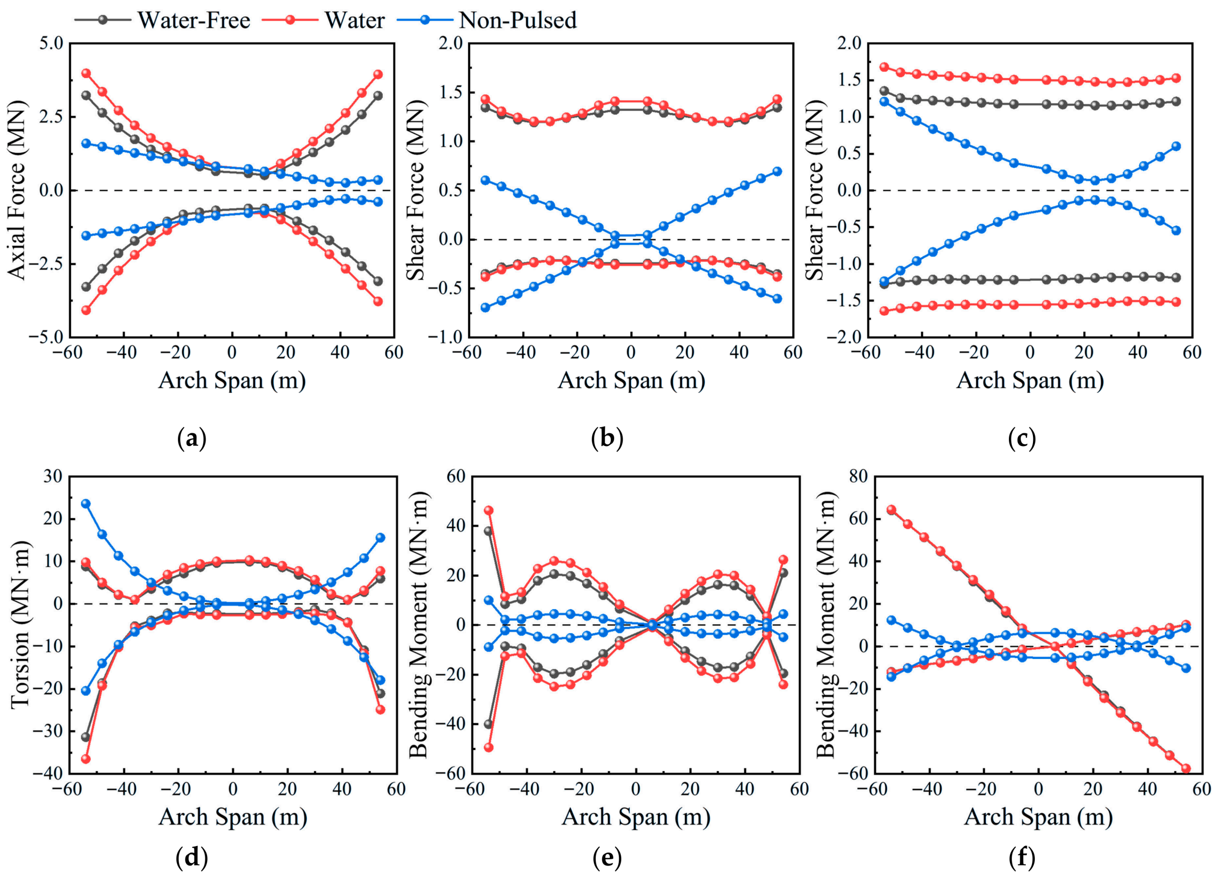

Figure 13. Comparison of Arch Ring Internal Forces: (**a**) Axial Force; (**b**) Lateral Shear Force; (**c**) Vertical Shear Force; (**d**) Torsion; (**e**) Lateral Bending Moment; (**f**) Vertical Bending Moment.

On the other hand, Figure 13 also shows that the internal force response of the arch ring under non-pulse seismic excitation is significantly lower than under pulse-type seismic excitation. At key sections, pulse-type earthquakes not only significantly increase the internal forces in the arch ring but may also lead to damage modes different from those induced by non-pulse earthquakes.

This conclusion is further verified in Figures 14–16, which show the displacement of the arch ring, the displacement of the vertical supports, and the displacement of the main beam, respectively. The results indicate that the presence or absence of water in the pipeline has little effect on the structural displacement, with slightly higher displacements observed when the pipeline contains water. Furthermore, the structural response under pulse-type earthquakes is significantly higher than under non-pulse-type earthquakes. In particular, under the influence of low-frequency pulses, the response of the 2# arch support and the main beam in the second span is significantly amplified under pulse-type seismic excitation, while no such phenomenon is observed under non-pulse seismic excitation. Lateral displacement also shows significant differences between the two types of earthquakes, with the displacement under pulse-type earthquakes being considerably greater than under non-pulse-type earthquakes. In conclusion, the added water in the pipeline significantly increases the internal forces in the siphon bridge structure. Considering the effects of pulse-type seismic motions on the structural seismic response is crucial for improving the ductility design of the siphon bridge structure, thereby enhancing its seismic performance.

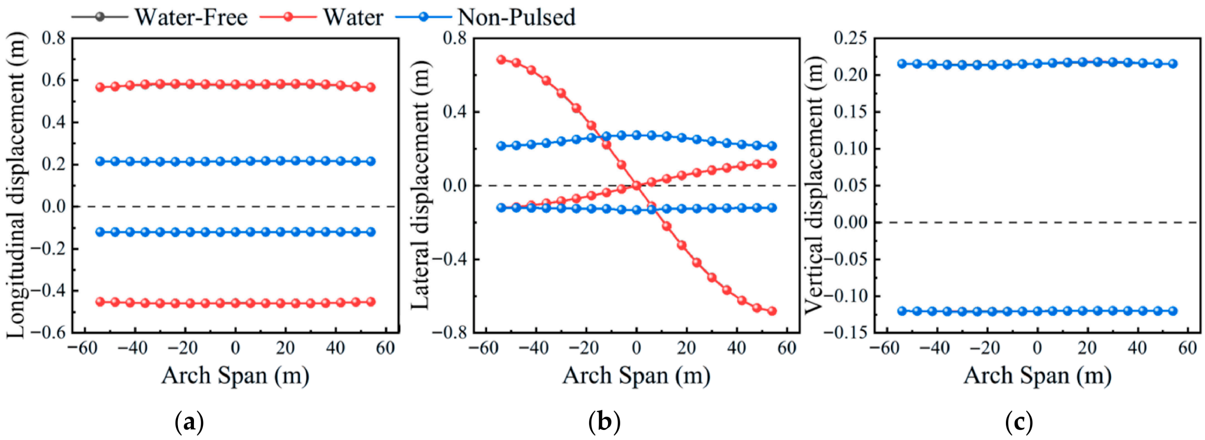

Figure 14. Arch Ring Displacement: (**a**) Longitudinal Displacement; (**b**) Lateral Displacement; (**c**) Vertical Displacement.

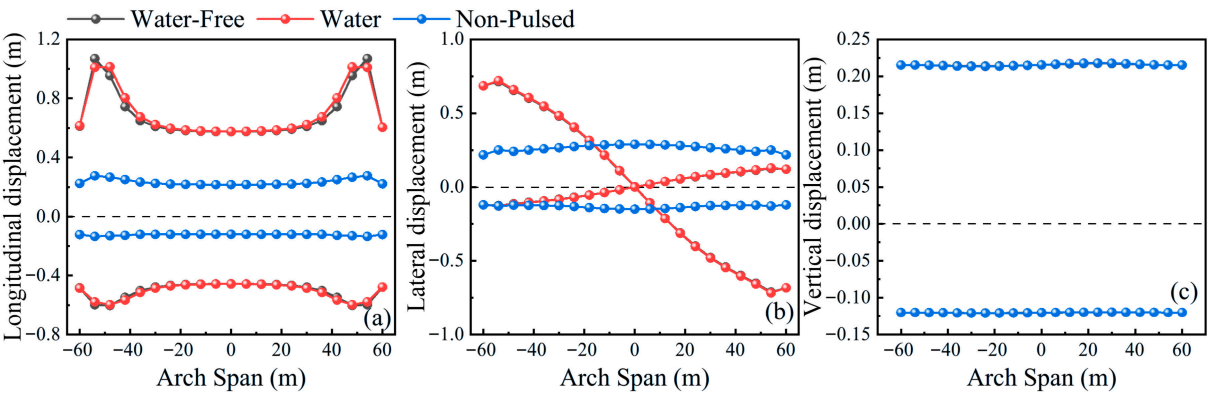

Figure 15. Vertical Support Displacement: (**a**) Longitudinal Displacement; (**b**) Lateral Displacement; (**c**) Vertical Displacement.

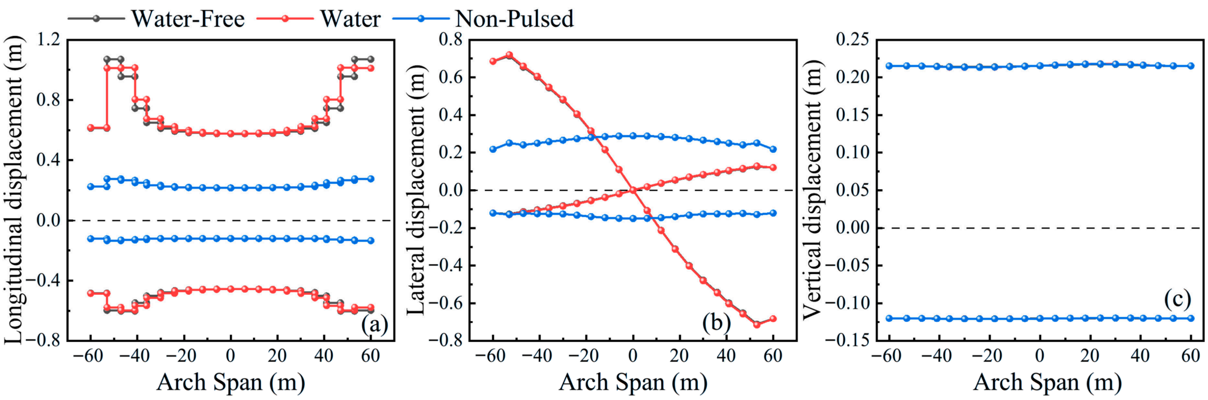

Figure 16. Comparison of Main Beam Displacement: (**a**) Longitudinal Displacement; (**b**) Lateral Displacement; (**c**) Vertical Displacement.

6. Discussion

The numerical results indicate that the seismic response of the fault-crossing siphon arch bridge is strongly governed by the combined effects of permanent displacement, pulse-frequency characteristics, and water added mass. First, the phase-angle analysis shows that the most unfavorable structural response occurs when the phase angle is close to 0°, which is mainly associated with the larger transverse permanent-displacement component. This suggests that, for fault-crossing siphon bridges, the displacement-controlled effect induced by fault movement may play a more dominant role than conventional acceleration-dominated seismic demand.

Second, the frequency-parameter analysis shows that the structural response is highly sensitive to pulse frequency when it approaches the dominant modal frequencies of the bridge. The vertical supports and the main beam are mainly sensitive to longitudinal vibration modes, whereas the arch ring is more sensitive to the lateral symmetric mode. This result implies that the dynamic characteristics of different structural components should be explicitly considered in the seismic assessment of siphon bridge systems under pulse-type fault-crossing ground motions.

Third, the comparison between the full-water and no-water conditions demonstrates that the added mass of water significantly changes the dynamic properties of the structure and amplifies the internal-force response of key sections. This finding highlights that neglecting the water mass may lead to an underestimation of seismic demand in siphon bridge structures. In addition, the comparison between pulse-type and non-pulse seismic inputs shows that pulse-type fault-crossing motions may produce much larger response demands and potentially different damage patterns.

It should also be noted that the present study is based on several simplifying assumptions, including the rigid-foundation assumption and the use of the added-mass method to represent the water effect. Therefore, the results should be interpreted as a preliminary evaluation of the global seismic response of the fault-crossing siphon arch bridge. More refined analyses considering soil–structure interaction and detailed fluid–structure coupling should be conducted in future work.

7. Conclusions

Based on the time-history analysis of the siphon arch bridge subjected to pulse-type fault-crossing ground motions, the following conclusions can be drawn:

(1) As the pulse phase angle increases from 0° to 90°, both the displacement and internal-force responses of the structure generally decrease. The most unfavorable condition occurs at 0°, indicating that fault-induced permanent displacement plays a dominant role in the seismic demand of the fault-crossing siphon arch bridge.

(2) Significant response amplification occurs when the pulse frequency approaches the dominant modal frequencies of the structure. In the present case, the arch ring is particularly sensitive near the lateral dominant mode at about 0.439 Hz, while the vertical supports and the main beam are mainly sensitive near the longitudinal dominant modes at about 0.345 Hz and 0.51 Hz.

(3) Filling the siphon pipeline with water reduces the first five natural frequencies from 0.369, 0.369, 0.487, 0.542, and 0.552 Hz to 0.326, 0.326, 0.445, 0.475, and 0.484 Hz, respectively, corresponding to a reduction of about 8–14%. Under the most unfavorable case, the maximum axial force, lateral shear force, vertical shear force, torsion, lateral bending moment, and vertical bending moment of the arch ring increase by approximately 29.2%, 6.6%, 238%, 21.8%, 55.9%, and 30.9%, respectively, compared with the no-water condition.

(4) Compared with non-pulse seismic excitation, pulse-type fault-crossing ground motions produce markedly larger structural responses, especially in critical components such as the arch bottom, the 2# vertical support, and the main beam near the second span, indicating that pulse-type input may lead to more unfavorable force concentration and deformation demand in the siphon bridge system.

https://doi.org/10.3390/civileng7020032

Author Contributions: Conceptualization, Y.O. and P.L.; validation, T.W.; formal analysis, X.L.; resources, Y.C.; funding acquisition, X.Z.; Writing—original draft, Y.O. and X.L.; Writing—review & editing, X.Z. All authors have read and agreed to the published version of the manuscript.

Funding: This study was supported by the Sichuan Science and Technology Program (grant No. 2025ZNSFSC0411).

Data Availability Statement: The raw data supporting the conclusions of this article will be made available by the authors on request.

Conflicts of Interest: Authors Yupeng Ou, Pingan Liu, Youlin Chen and Tiehu Wang were employed by the company Power China Chengdu Engineering Corporation Limited. The remaining authors declare that the research was conducted in the absence of any commercial or financial relationships that could be construed as a potential conflict of interest.

References

1. Mavroeidis, G.P.; Papageorgiou, A.S. A mathematical representation of near-fault ground motions. *Bull. Seismol. Soc. Am.* **2003**, *93*, 1099–1131. [CrossRef]
2. Mavroeidis, G.P.; Dong, G.; Papageorgiou, A.S. Near-fault ground motions and the response of elastic and inelastic single-degree-of-freedom systems. *Earthq. Eng. Struct. Dyn.* **2004**, *33*, 1023–1049. [CrossRef]
3. Bray, J.D.; Rodriguez-Marek, A. Characterization of forward-directivity ground motions in the near-fault region. *Soil Dyn. Earthq. Eng.* **2004**, *24*, 815–828. [CrossRef]
4. Youngs, R.R.; Arabasz, W.J.; Anderson, R.E.; Ramelli, A.R.; Ake, J.P.; Slemmons, D.B.; McCalpin, J.P.; Doser, D.I.; Fridrich, C.J.; Swan, F.H., III; et al. A methodology for probabilistic fault displacement hazard analysis (PFDHA). *Earthq. Spectra* **2003**, *19*, 191–219. [CrossRef]
5. Hisada, Y.; Bielak, J. A theoretical method for computing near-fault ground motions in layered half-spaces considering static offset due to surface faulting, with a physical interpretation of fling step and rupture directivity. *Bull. Seismol. Soc. Am.* **2003**, *93*, 1154–1168. [CrossRef]
6. Beresnev, I.A. Simulation of near-fault high-frequency ground motions from the representation theorem. *Pure Appl. Geophys.* **2017**, *174*, 4021–4034. [CrossRef]
7. Rupakhety, R.; Sigurdsson, S.U.; Papageorgiou, A.S.; Sigbjörnsson, R. Quantification of ground-motion parameters and response spectra in the near-fault region. *Bull. Earthq. Eng.* **2011**, *9*, 893–930. [CrossRef]
8. Katsimpini, P.S.; Papagiannopoulos, G.; Hatzigeorgiou, G. Nonlinear Analysis of Bridges Considering Soil-Structure In-teraction and Travelling Wave Effects Under Combined Train and Near-Fault Seismic Loads. *Appl. Sci.* **2024**, *14*, 11688. [CrossRef]
9. O'Rourke, M.J.; Liu, X. *Response of Buried Pipelines Subject to Earthquake Effects*; MCEER: New York, NY, USA, 1999.
10. Melissianos, V.E.; Vamvatsikos, D.; Gantes, C.J. Performance assessment of buried pipelines at fault crossings. *Earthq. Spectra* **2017**, *33*, 201–218. [CrossRef]
11. Dabaghi, M.; Der Kiureghian, A. Stochastic model for simulation of near-fault ground motions. *Earthq. Eng. Struct. Dyn.* **2017**, *46*, 963–984. [CrossRef]
12. Dabaghi, M.; Der Kiureghian, A. Simulation of orthogonal horizontal components of near-fault ground motion for specified earthquake source and site characteristics. *Earthq. Eng. Struct. Dyn.* **2018**, *47*, 1369–1393. [CrossRef]
13. Peng, Y.; Luo, C.; Qiu, C.; Kong, F. Stochastic simulation of velocity pulses of near-fault ground motions based on multivariate copula modeling. *Probabilistic Eng. Mech.* **2023**, *72*, 103434. [CrossRef]
14. Luo, C.; Peng, Y. Probability density evolution method based stochastic simulation of near-fault pulse-like ground motions. *Probabilistic Eng. Mech.* **2024**, *76*, 103629. [CrossRef]
15. Zhang, C.; Wu, C.; Wang, P.; Li, D.; Lu, J. Improved methods for synthesizing near-fault ground motions based on specific response spectrum. *Soil Dyn. Earthq. Eng.* **2024**, *183*, 108790. [CrossRef]
16. Jiang, X.H.; Hong, H.P.; Ren, J.D. Simulating multi-component near-fault ground motion record containing pulse-like component. *Soil Dyn. Earthq. Eng.* **2025**, *188*, 109032. [CrossRef]
17. Luo, Q.; An, J.; Wang, Z. Synthesis of time-frequency non-stationary stochastic near-fault fling-step ground motion based on time-frequency non-stationary ground motion model and stochastic pulse model. *Soil Dyn. Earthq. Eng.* **2025**, *188*, 109094. [CrossRef]
18. Liu, X.; Zhang, X.; Zhang, J.; Kong, D.; Wan, X. A stochastic synthesis method for near-fault ground motions incorporating fling-step effects. *Soil Dyn. Earthq. Eng.* **2026**, *203*, 110098. [CrossRef]
19. Shi, C.; Cheng, C.; Wang, Z.; Wu, H.; Hu, Y. Seismic performance of large-span siphon pipeline bridge structures. *J. Yangtze River Sci. Res. Inst.* **2022**, *39*, 111–116.

20. Forcellini, D.; Kalfas, K. A framework to quantify the impact of deterioration on the seismic resilience of structures. *Struct. Infrastruct. Eng.* **2025**, 1–9, *advance online publication*. [CrossRef]
21. Kameshwar, S.; Forcellini, D.; Barbosa, A.R. Assessment of building recovery functions for local and global resilience assessment to tsunamis. *Resilient Cities Struct.* **2025**, *4*, 132–145. [CrossRef]
22. Du, A.; Wang, X.; Xie, Y.; Dong, Y. Regional seismic risk and resilience assessment: Methodological development, applicability, and future research needs—An earthquake engineering perspective. *Reliab. Eng. Syst. Saf.* **2023**, *233*, 109104. [CrossRef]
23. Ní Choine, M.; O'Connor, A.J.; Padgett, J.E. Comparison between the seismic performance of integral and jointed concrete bridges. *J. Earthq. Eng.* **2015**, *19*, 172–191. [CrossRef]
24. Wang, J.; Zhang, H.; Yang, S.; Wu, Y.; Luo, B.; Liao, Y. Seismic performance of inverted siphon bridge with isolation bearing: Insights from shaking table tests. *Structures* **2025**, *81*, 110365. [CrossRef]
25. Wu, Y.; Wang, J.; Gao, Y.; Yang, S.; Liao, Y.; Luo, B. Shaking table test of arch bridge inverted siphon considering different pulse parameters of near-fault ground motions. *Eng. Struct.* **2025**, *327*, 119619. [CrossRef]
26. Zhou, D.; Li, R.; Cui, Y.; Li, X.; Luo, S. Seismic response analysis of large-span, large-section arch inverted siphon bridges. *Eng. Seismol. Strength. Reinf.* **2023**, *45*, 126–134.
27. Li, D.; Li, Y.; Bai, R.; Chen, J. Comparative study of ground pressure pipe structure types for fault-crossing inverted siphon systems. *People's Yangtze River* **2024**, *55*, 171–178.
28. Xie, X.; Li, R.; Cui, Y.; Li, X.; Luo, S. Dynamic response analysis of an inverted siphon pipeline water hammer pressure wave and arch bridge structure based on bidirectional fluid–structure coupling. *J. Appl. Mech.* **2024**, *41*, 466–476.
29. Wang, Y.; Zhang, Y.; Huang, Z.; Wang, K.; Tang, A. Seismic response characteristics of a utility tunnel crossing a river considering hydrodynamic pressure effects. *Buildings* **2024**, *14*, 3434. [CrossRef]
30. Shi, Y.; Xu, L.; Hou, R.; Zhang, D.; Zhang, D. Seismic response and damage analysis of large inverted siphon structure. *Shock Vib.* **2022**, *2022*, 5404908. [CrossRef]
31. Jiang, L.; Liao, Y.; Wang, Z.; Wu, Y.; Li, M. Seismic response analysis of arch inverted siphon under differential seismic effects in a valley. *J. Yangtze River Sci. Res. Inst.* **2022**, *39*, 117–121.
32. Xin, L.; Li, X.; Zhang, Z.; Zhao, L. Seismic behavior of long-span concrete-filled steel tubular arch bridge subjected to near-fault fling-step motions. *Eng. Struct.* **2019**, *180*, 148–159. [CrossRef]
33. Xiong, L.; Zhou, W.; Jiang, L. Seismic risk transfer in multi-span simply supported beam bridges for high-speed railways. *Soil Dyn. Earthq. Eng.* **2025**, *188*, 109057. [CrossRef]
34. Scott, B.D.; Park, R.; Priestley, M.J.N. Stress-strain behavior of concrete confined by overlapping hoops at low and high strain rates. *J. Proc.* **1982**, *79*, 13–27.
35. Lin, Y.; Chen, Y.; Zong, Z.; Bi, K. A state-of-the-art review of bridges subjected to earthquake fault ruptures. *Eng. Struct.* **2025**, *330*, 119889. [CrossRef]
36. Liu, Z.; Liu, W.; Peng, Y. Random function based spectral representation of stationary and non-stationary stochastic processes. *Probabilistic Eng. Mech.* **2016**, *45*, 115–126. [CrossRef]
37. Lin, Y.K.; Yong, Y. Evolutionary Kanai–Tajimi earthquake models. *J. Eng. Mech.* **1987**, *113*, 1119–1137. [CrossRef]
38. Tang, Y.; Zhang, J. Response spectrum-oriented pulse identification and magnitude scaling of forward directivity pulses in near-fault ground motions. *Soil Dyn. Earthq. Eng.* **2011**, *31*, 59–76. [CrossRef]
39. Baker, J.W. Quantitative classification of near-fault ground motions using wavelet analysis. *Bull. Seismol. Soc. Am.* **2007**, *97*, 1486–1501. [CrossRef]
40. Shahi, S.K.; Baker, J.W. An efficient algorithm to identify strong-velocity pulses in multicomponent ground motions. *Bull. Seismol. Soc. Am.* **2014**, *104*, 2456–2466. [CrossRef]
41. Liu, Z.; Liu, Z.; Chen, D. Probability density evolution of a nonlinear concrete gravity dam subjected to nonstationary seismic ground motion. *J. Eng. Mech.* **2018**, *144*, 04017157. [CrossRef]
42. Yang, D.; Zhou, J. A stochastic model and synthesis for near-fault impulsive ground motions. *Earthq. Eng. Struct. Dyn.* **2015**, *44*, 243–264. [CrossRef]
43. *GB 51247-2018*; Standard for Seismic Design of Hydraulic Structures. China Planning Press: Beijing, China, 2018.

https://doi.org/10.3390/civileng7020032